A review of molecule-based conductors electrodeposited as thin films on silicon wafers

2008 J. Phys.: Condens. Matter 20 184012

(http://iopscience.iop.org/0953-8984/20/18/184012)

IOP PUBLISHING JOURNAL OF PHYSICS: CONDENSED MATTER

J. Phys.: Condens. Matter **20** (2008) 184012 (10pp) doi:10.1088/0953-8984/20/18/184012

A review of molecule-based conductors electrodeposited as thin films on silicon wafers

Dominique de Caro, I Malfant, J-P Savy and L Valade

Laboratoire de Chimie de Coordination (CNRS UPR 8241), 205, route de Narbonne, 31077 Toulouse Cedex 4, France

E-mail: decaro@lcc-toulouse.fr

Received 4 September 2007, in final form 5 December 2007
Published 17 April 2008
Online at stacks.iop.org/JPhysCM/20/184012

Abstract

A tremendous effort has been devoted in the past three decades to the preparation and study of molecule-based conductors derived from organic, organometallic or metallorganic species. The work described in this paper reviews examples of thin films of these systems electrodeposited on intrinsic (001)-oriented silicon wafers.

1. Introduction

For the past three decades, the electrocrystallization technique has been used extensively to prepare a large variety of molecule-based conductors and superconductors [1, 2]. Single crystals of high purity are usually obtained on a wire-like electrode. However, it is difficult to envision a technological breakthrough by using such single crystals. Thin films deposited on a large area electrode offer a more convenient morphology. To our knowledge, the first example describing the thin film processing of a charge-transfer salt is the epitaxial growth of β-(BEDT-TTF)$_2$I$_3$ on a graphite substrate (BEDT-TTF: bis(ethylenedithiotetrathiafulvalene)) reported by Ward *et al* [3]. *In situ* atomic force microscopy reveals that a monolayer of β-(BEDT-TTF)$_2$I$_3$ forms upon the application of an anodic potential. A few years later the electrodeposition of $[(n\text{-}C_4H_9)_4N]_{0.9}[Ni(dmid)_2]$ on a Pt metal foil with galvanostatic conditions was described ($dmid^{2-}$: 1,3-dithiole-2-one-4,5-dithiolate) [4]. Amorphous films are obtained and show reproducible bistable electrical switching and memory phenomena. More recently, conductive thin films of (BEDT-TTF)$(ClO_4)_x$ have been constructed by a successive dry–wet process, combining the ultra-high vacuum deposition of neutral BEDT-TTF molecules and an electrochemical doping process using an aqueous solution of $LiClO_4$ as the electrolyte [5]. Finally, Wang *et al* reported the electrochemical preparation of thin films [6] and surface patterns [7] of BEDT-TTF derivatives on gold or gold-on-mica substrates. Our group has developed an electrodeposition technique using large area silicon wafers as anodes to prepare thin films of molecule-based conductors. The silicon affords evident benefits versus platinum or gold in terms of maintenance and cost. We considered two different goals: (i) growth of a thin film and (ii) large scale preparation. The first goal is of interest for future applications, silicon being the substrate of choice in the electronic domain. The second goal is extremely useful to prepare the large amounts of product (several hundreds of milligrams) often required for physical measurements. This paper reviews the preparation of organic and metallorganic conductor films on intrinsic (001)-oriented silicon electrodes. Silicon pre-treatment and electrolysis conditions are detailed in the corresponding references. However, data concerning the applied current density, the electrodeposition duration, and the morphology of the film are gathered in table 1. Moreover, molecular formulas for molecules cited in the text are shown in scheme 1.

2. Superconducting phases

2.1. *TTF*[*Ni*(*dmit*)$_2$]$_2$

TTF[Ni(dmit)$_2$]$_2$ belongs to the donor–acceptor family of compounds (TTF: tetrathiafulvalene; $dmit^{2-}$: 1,3-dithiole-2-thione-4,5-dithiolato). The charge transfer between the TTF donor molecule and the [Ni(dmit)$_2$] acceptor complex was found to be 0.80 from diffuse x-ray scattering experiments and band structure calculations [8]. Single crystals exhibit a room temperature conductivity of 300 S cm^{-1}. The conductivity behavior is metallic down to 4 K and this compound undergoes a complete transition to a superconducting state at 1.6 K under a hydrostatic pressure of 7 kbar [9].

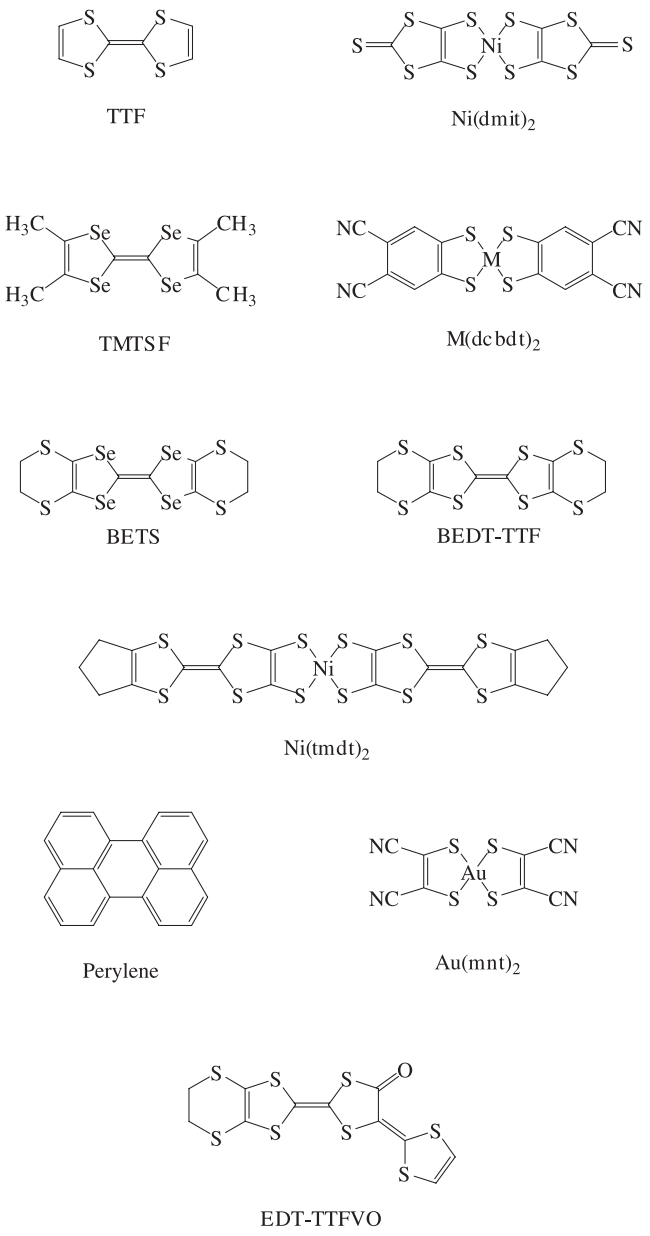

Scheme 1. Molecular formulas.

TTF[Ni(dmit)$_2$]$_2$ films are electrodeposited on silicon from a 3:1 molar ratio of the TTF and [(n-C$_4$H$_9$)$_4$N][Ni(dmit)$_2$] starting materials in acetonitrile. An effect of current density on morphology has been evidenced (figure 1). At low current density (1.5 μA cm^{-2}), deposits show a grain-like morphology (sample 1). The grain size ranges from 0.6 to 1 μm [10]. It is to be noticed that ∼15% of the silicon surface remains uncovered. By applying a higher current density (∼6.2 μA cm^{-2}), films are made of fibers, arranged as bundles, and typically 1–2 μm wide and 20–60 μm long (sample 2) [11]. This latter morphology mimics that obtained for single crystals, i.e. needle-like morphology. X-ray diffraction patterns of the deposits are in good agreement with the simulation calculated using single crystal data (space group $C_{2/c}$; $a = 4.621$ nm; $b = 0.373$ nm; $c = 2.282$ nm; $\alpha = \gamma = 90°$; $\beta = 119.24°$). The x-ray photoelectron spectroscopy S 2p line can be satisfactorily decomposed into three contributions. According to their relative intensities, the most intense line, with a binding energy of 163.5 eV, corresponds to C–S–C bonds. Lines at 161.8 and 165.3 eV correspond to C–S–Ni and C=S bonds, respectively. In the nominal formula TTF[Ni(dmit)$_2$]$_2$, there are 12 C–S–C, eight C–S–Ni and four C=S bonds, which results in a 3:2:1 ratio. The experimental intensity ratio between the C–S–C and C–S–Ni contributions is 1.4, in excellent agreement with the nominal 1.5 value. Infrared and Raman spectra for the deposits are very similar to those performed on single crystals. In the 1300–1650 cm^{-1} range, Raman spectra are dominated by $\nu_{C=C}$ stretching modes. The higher intensity line (1436 cm^{-1}), involving a large contribution of the central carbon–carbon double bond in TTF (71%), allows the determination of the amount of charge transfer [12]. For the films, a charge transfer of about 0.86 has been found. This is in relatively good agreement with the value obtained on single crystals (0.80). Figure 2 shows the electrical behavior for sample 1. The normalized resistance is reported as a function of the temperature. Sample 1 exhibits a metallic behavior down to ca. 14 K, a temperature at which the resistance slightly increases. At 14 K, the resistance is around 4.3 times smaller than the resistance at 300 K, and it is still four times smaller at 4.5 K. Such a behavior is totally reversible when warming back to room temperature. Sample 1 was not further studied at lower temperatures because it develops cracks due to mechanical stresses at cryogenic temperatures. Resistivity measurements on sample 2 have been performed between ambient pressure and 7.7 kbar. Whatever the pressure value, the resistance is nearly constant in the 100–300 K range, and significantly increases below 100 K. Between 100 and 300 K, inter-fiber contacts do not affect too much the overall electrical behavior of the film. They become more resistive below 100 K and explain the semiconducting behavior observed below this temperature. The room-temperature conductivity is about 9 S cm^{-1} (at ambient pressure) and 24 S cm^{-1} (under 7.7 kbar). Moreover, the slope, $\frac{1}{\sigma_{1\mathrm{bar}}}\frac{\mathrm{d}\sigma}{\mathrm{d}P} \sim 0.28$ kbar^{-1}, is remarkably similar to the value measured on single crystals [13]. This evidences that the influence of the inter-fiber resistance is not a limiting factor to probe the intrinsic properties of the compound. For sample 2, superconductivity is manifested by a broad drop of the resistance below 0.8 K, as illustrated in figure 3. However, the transition observed is incomplete (versus complete for single crystals along the stacking direction), presumably due to the contributions of grain boundaries. The effective presence of superconductivity has been confirmed by the application of a magnetic field perpendicular to the plane of the film. At 1.9 T, the transition is no longer observed. The critical field is estimated to be 0.45 T, a lower value versus single crystals (2.5 T) due to inter-fiber resistance contributions. Although incomplete, the evidence of a superconducting transition for a thin molecular film constitutes a promising result.

2.2. $(TMTSF)_2ClO_4$

TMTSF (tetramethyltetraselenafulvalene) is the base component of the Bechgaard salts, a series of quasi-one-dimensional conductors with general formula (TMTSF)$_2$X, where X stands

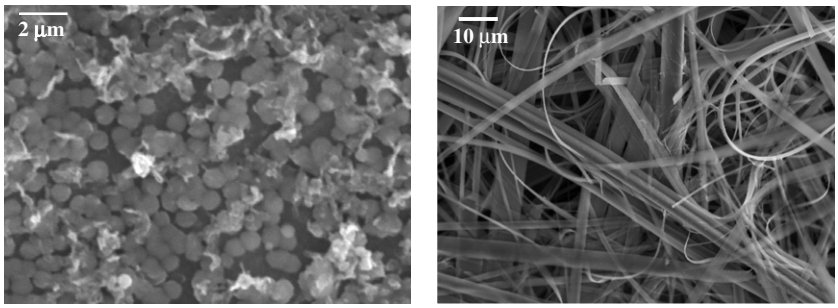

Figure 1. Scanning electron micrographs for samples 1 (left) and 2 (right).

Table 1. Experimental conditions and morphology for thin films of molecule-based conductors.

Sample	Current density (μA cm^{-2})	Solvent	Electrodeposition duration (days)	Morphology
1	1.5	CH_3CN	5	Roughly spherical grains
2	6.2		15	Micro-fibers
3	15	Cl_2HC–CH_2Cl	2	Blocks
4	25		2	Blocks
5	40		10	Micro-needles
6	0.5	CH_2Cl_2	4	Thin platelets
7	1.0		2	Continuous film
8	1.6	CH_2Cl_2	3	Micro-fibers
9	1.0		10	Thin platelets
10	1.4		4	Thin platelets
11	1.0	CH_3CN	3	Stacked sheets
12	0.1	Cl_2HC–CH_2Cl/C_2H_5OH	2	Thin platelets
13	2.5	CH_2Cl_2	10	Long needles
14	2.5	CH_3CN	5	Flakes
15	0.3	CH_2Cl_2	3	Nanowires
16	0.15	C_6H_5Cl/C_2H_5OH	10	Nanowires

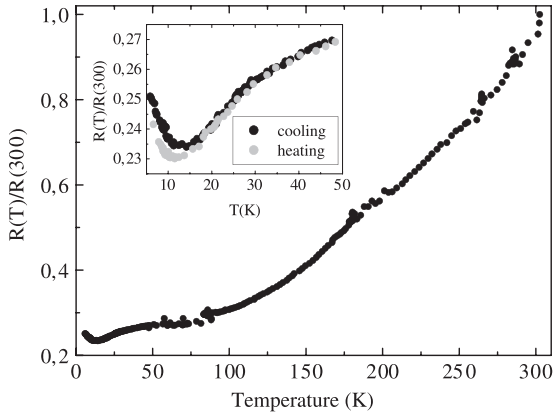

Figure 2. Temperature evolution of the electrical resistance normalized to the resistance at 300 K for sample 1.

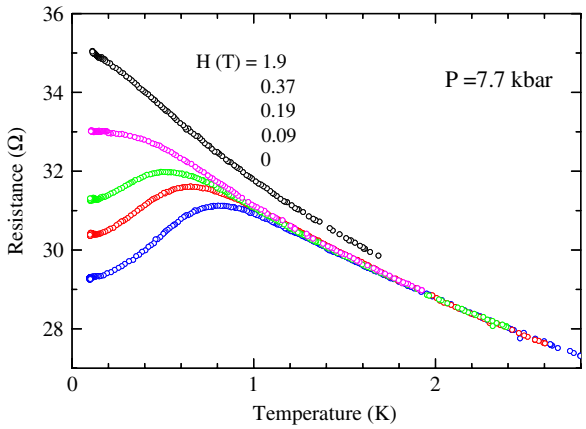

Figure 3. Temperature dependence of the resistance of sample 2 at $P = 7.7$ kbar, in the superconducting domain, for different applied magnetic fields ranging from 0 (down curve) to 1.9 T (top curve). (This figure is in colour only in the electronic version)

for monovalent inorganic anion. The first discovered ambient pressure organic superconductor was $(TMTSF)_2ClO_4$ with $T_c = 1.2$ K [14]. An interesting approach to the preparation of $(TMTSF)_2ClO_4$ thin films was described by Ribault *et al* [15]. They performed the epitaxial electrodeposition of $(TMTSF)_2ClO_4$ onto a $(TMTSF)_2PF_6$ isostructural template in dichloromethane solution ($j \sim 0.12$ μA cm^{-2}). As-generated $(TMTSF)_2ClO_4$ overlayers on $(TMTSF)_2PF_6$ single crystals were found to be superconducting [16]. By applying such low current densities in a 1,1,2-trichloroethane solution containing TMTSF and $[(n\text{-}C_4H_9)_4N]ClO_4$, no deposit is obtained on Si, and decomposition of TMTSF occurs after several days' electrolysis.

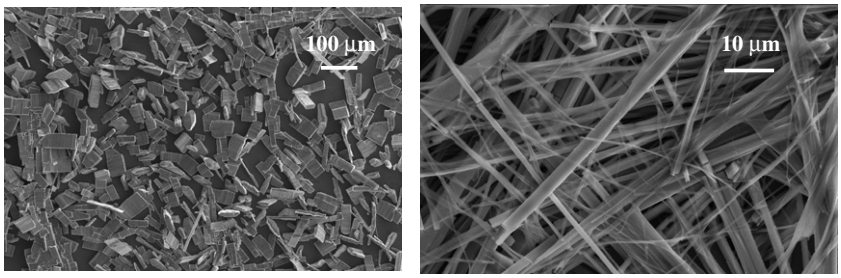

Figure 4. Scanning electron micrographs for samples 4 (left) and 5 (right).

The $(TMTSF)_2ClO_4$ phase can be grown on the silicon electrode using much higher current densities (in the 15–40 $\mu A\,cm^{-2}$ range) [17]. As in the case of $TTF[Ni(dmit)_2]_2$, an effect of the current density on morphology is observed. At 15 $\mu A\,cm^{-2}$ (sample 3) and 25 $\mu A\,cm^{-2}$ (sample 4), blocks displaying various shapes are observed (size ranging from 10 to 100 μm; figure 4). At 40 $\mu A\,cm^{-2}$ (sample 5), long needles are observed (length $>$ 150 μm, figure 4), a morphology in agreement with the quasi-one-dimensional character of $(TMTSF)_2ClO_4$ considering that growth under an electroactivated process is favored along the higher conductive path. For samples 3 and 4, the silicon surface was not covered enough to perform x-ray diffraction measurements. For sample 5, Bragg peaks can be assigned to the triclinic known phase (space group $P\bar{1}$; $a = 7.231$ nm; $b = 7.539$ nm; $c = 13.281$ nm; $\alpha = 84.11°$; $\beta = 87.03°$; $\gamma = 70.77°$). Additional peaks which have yet to be indexed are observed. They correspond neither to neutral TMTSF nor to the monoclinic μ''-$(TMTSF)_2ClO_4$ prepared by confined electrocrystallization [18]. X-ray photoelectron spectroscopy of the $(TMTSF)_2ClO_4$ films shows the presence of Se, C and O. The Se(3d), $Se(3p_{3/2})$ and $Se(3p_{1/2})$ lines are located at 55.9, 161.9 and 167.7 eV, respectively. These values are close to those obtained on neutral TMTSF pressed pellets under the same experimental conditions (56.0, 162.2 and 167.9 eV). However, for the deposits, the selenium lines are systematically broader than the same lines measured on neutral TMTSF. This might be taken as an indirect proof of the charge transfer, as observed in several BEDT-TTF salts. Infrared and Raman spectra recorded on samples 3, 4 and 5 are identical to those performed on $(TMTSF)_2ClO_4$ single crystals. Infrared spectra are dominated by a strong absorption located at 1092 cm^{-1}, which is assigned to the ClO_4^- anion. Raman modes dominated by the C=C stretches (1462 and 1600 cm^{-1}) display a large shift by comparison to neutral TMTSF (1539 and 1625 cm^{-1}). The position of the more intense signal (1462 cm^{-1}) is in good agreement with a 0.5 formal charge borne by the TMTSF donor. Samples 3 and 4 have similar electrical behaviors. Figure 5 shows the temperature variation of the electrical resistance normalized to the resistance at 160 K. The films' conductivity exhibits a thermo-activated behavior, evidencing the limiting effect caused by grain boundaries. Note that at 24 K the curve shows a minimum and that the resistance versus temperature slope increases below this temperature. This discontinuity can be associated with the anion-ordering transition [19]. At temperatures lower than 22 K, resistance values were too fluctuating to envision observation of the superconducting transition. Finally, in the 4–300 K range, resistivity measurements for sample 5 are too unstable to be discussed.

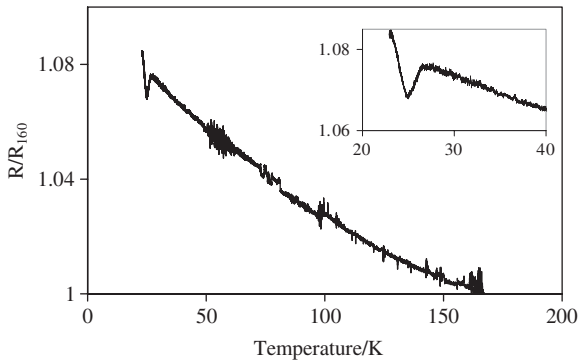

Figure 5. Temperature evolution of the electrical resistance normalized to the resistance at 160 K for sample 4.

3. Metal–dicyanobenzodithiolate derivatives

3.1. $[(n\text{-}C_4H_9)_4N]_2[M(dcbdt)_2]_5$

The synthesis of $M(dcbdt)_2$ complexes ($dcbdt^{2-}$: 4,5-dicyanobenzene-1,2-dithiolato) opened the route to a novel family of molecule-based conductors. The presence of a relatively large and extended π-system within the $dcbdt^{2-}$ ligand makes the complexes relatively easy to oxidize. $[(n\text{-}C_4H_9)_4N]_2[M(dcbdt)_2]_5$ (M = Ni, Au) single crystals can be prepared as thin plates ($3 \times 0.3 \times 0.05$ mm^3) on a platinum wire, by electrocrystallization from the corresponding $[(n\text{-}C_4H_9)_4N][M(dcbdt)_2]$ complex under galvanostatic conditions [20, 21]. Both compounds present a triclinic structure ($P\bar{1}$) showing stacks of pentamerized $M(dcbdt)_2$ units. The electrical conductivity measured along the long axis (stacking axis) of the elongated-shaped crystals denotes a semiconducting behavior ($\sigma_{RT} = 0.13$ S cm^{-1} and activation energy $E_a = 0.176$ eV for M = Ni; $\sigma_{RT} = 10$ S cm^{-1} and $E_a = 0.027$ eV for M = Au).

Thin films of $[(n\text{-}C_4H_9)_4N]_2[M(dcbdt)_2]_5$ (M = Ni, Au) are obtained by galvanostatic electrolysis on a silicon wafer in an electrochemical cell containing a dichloromethane solution of $[(n\text{-}C_4H_9)_4N][M(dcbdt)_2]$ [22]. For M = Ni (sample 6, figure 6), electron micrographs evidence that the film is made

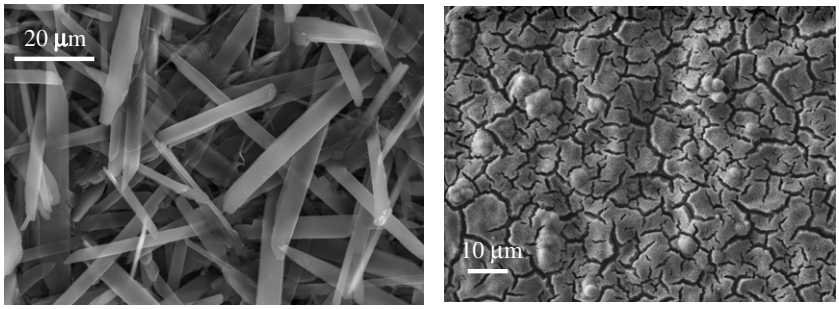

Figure 6. Scanning electron micrographs for samples 6 (left) and 7 (right).

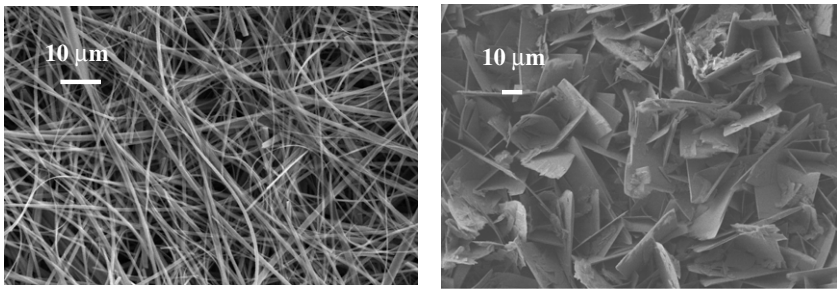

Figure 7. Scanning electron micrographs for samples 8 (left) and 10 (right).

of thin platelets (30–55 μm long, 1–8 μm width, thickness <1 μm) randomly distributed on the silicon surface. For M = Au (sample 7, figure 6), a continuous film is observed. The adherence of the film onto the Si substrate is not affected by the presence of cracks. Elemental analysis of a sample of film scratched from the surface is in good agreement with the data calculated for $[(n\text{-}C_4H_9)_4N]_2[M(dcbdt)_2]_5$. X-ray powder diffraction of sample 6 (M = Ni) evidences a highly oriented film. Refinement of the collected data gives the following crystallographic parameters: $a = 0.800$ nm, $b = 1.727$ nm, $c = 2.249$ nm, $\alpha = 69.01°$, $\beta = 89.08°$, $\gamma = 78.90°$, to be compared with $a = 0.800$ nm, $b = 1.728$ nm, $c = 2.249$ nm, $\alpha = 69.18°$, $\beta = 89.16°$, $\gamma = 78.14°$ obtained from single crystal study. The very good agreement of the lattice parameters shows that the deposition process does not affect the structural arrangement of the compound. Sample 7 (M = Au) is amorphous. The XPS spectrum for the N 1s line exhibits two components at 398.7 and 402.0 eV for Ni (399.3 and 403.1 eV for Au). The first peak arises from the cyano contribution of $M(dcbdt)_2$ while the second one corresponds to the tetrabutylammonium part. Raman spectra are identical to those recorded on single crystals. Intense Raman signals appearing at ∼1546 cm^{-1} (aromatic C=C stretching modes) and ∼2220 cm^{-1} (CN stretching modes) for precursor compounds shift to higher frequencies for the films (∼1557 and ∼2225 cm^{-1}, respectively). This frequency shift is in agreement with the decrease of the average value of the charge of the $M(dcbdt)_2$ moiety $[M(dcbdt)_2^- \rightarrow M(dcbdt)_2^{0.4-}]$. Samples 6 and 7 exhibit a semiconducting behavior ($E_a \sim 150$ meV). The room temperature conductivity of the films is at least one order of magnitude lower than that of single crystals: Ni, 1.2×10^{-2} S cm^{-1} versus 0.15 S cm^{-1}; Au, 6.0×10^{-2} S cm^{-1} versus 10 S cm^{-1}. For single crystals, conductivity measurements have been performed along the stacking direction, which is the direction of highest conductivity. The direction of highest conductivity is part of the plane in which the film conductivity is measured. This feature, the contributions of other directions within the crystallites and the polycrystalline nature of the film, which generates grain boundaries, account for the lower conductivity value of the film versus that of the crystal.

3.2. $(TMTSF)_x[M(dcbdt)_2]_y$

Charge-transfer derivatives combining a TTF-based donor (D) and $M(dcbdt)_2$ as an acceptor complex are not reported as single crystals. Electrocrystallization on a wire-like Pt electrode leads to amorphous powders of $D_x[M(dcbdt)_2]_y$ of unknown stoichiometries. Thin films of $(TMTSF)_x[M(dcbdt)_2]_y$ (M = Co, Ni, Au) are obtained by galvanostatic electrolysis on a silicon wafer in a cell containing a dichloromethane solution of TMTSF and $[(n\text{-}C_4H_9)_4N][M(dcbdt)_2]$. For M = Co (sample 8, figure 7), electron micrographs evidence that the film is made of microfibers (<3 μm wide, >100 μm long). For M = Ni and Au (samples 9 and 10, figure 7), films are made of thin platelets. Blocks (∼15 × 20 × 20 μm^3) are also occasionally encountered. The absence of diffraction peaks in the XRD pattern indicates that films either are amorphous or exhibit a nanocrystalline character. The x/y atomic ratio has been investigated using x-ray photoelectron spectroscopy. The TMTSF molecule bears four selenium atoms whereas the $M(dcbdt)_2$ moiety contains four sulfur atoms. Therefore, in $(TMTSF)_x[M(dcbdt)_2]_y$ phases, the

atomic Se/S ratio is equal to x/y. The BETS molecule (bis(ethylenedithio)tetrathiafulvalene) contains four selenium and four sulfur atoms in a similar chemical environment and can be used as a standard molecule. The XPS spectrum for BETS evidences Se 3s (230.7 eV) and S 2s (227.6 eV) signals, for which the area ratio corresponds to an atomic Se/S ratio of unity. Applying this area ratio factor to Se 3s and S 2s lines for $(TMTSF)_x[M(dcbdt)_2]_y$, x/y atomic ratios can be evaluated. The corresponding molecular formulas have been found: $(TMTSF)_5[Co(dcbdt)_2]_4$, $(TMTSF)[Ni(dcbdt)_2]$ and $(TMTSF)[Au(dcbdt)_2]$. Raman spectra for the deposits are dominated by the C=C stretching modes present in both TMTSF and $M(dcbdt)_2$ molecules. The most intense signal of the spectrum is the $\nu_4 a_g$ mode for TMTSF (1422 cm^{-1} for Co, 1397 cm^{-1} for Ni, 1397 cm^{-1} for Au). Its position follows a linear relationship with the charge borne by the TMTSF. The corresponding charges are the following: $TMTSF^{0.8+}$ for Co, $TMTSF^{+}$ for Ni and $TMTSF^{+}$ for Au. Assuming that the charge of the metal complex is -1, these results are in excellent agreement with stoichiometries determined by XPS. Moreover, $(TMTSF)[Ni(dcbdt)_2]$ and $(TMTSF)[Au(dcbdt)_2]$ behave as insulators, in agreement with a $TMTSF^{+}$ entity (empty valence band). $(TMTSF)_5[Co(dcbdt)_2]_4$ exhibits a semiconducting behavior ($E_a = 56$ meV; $\sigma_{RT} = 2$ S cm^{-1}), consistent with the fractional charge of TMTSF in this phase.

4. Multi-property compounds

4.1. $(TTF)_6[(C_2H_5)_4N](HPW_{12}O_{40})$

Polyoxometalates are currently of interest to build up organic/inorganic hybrid materials displaying multiple physical properties. Charge-transfer compounds combining an organic or an organometallic donor with an inorganic acceptor derived from a polyoxometalate structure ($M_6O_{19}^{2-}$ or $(XM_{12}O_{40})^{n-}$, M = Mo, W; X = P, Si, Ge ...) have been reported [23]. $(TTF)_6[(C_2H_5)_4N](HPM_{12}O_{40})$ (M = Mo, W) materials are prepared by the electrocrystallization technique, which consists in the oxidation of the organic donor (TTF) in the presence of tetraethylammonium salts of polyoxoanions in excess [24]. The two compounds, $(TTF)_6[(C_2H_5)_4N](HPMo_{12}O_{40})$ and $(TTF)_6[(C_2H_5)_4N](HPW_{12}O_{40})$, are isostructural. They present a semiconducting behavior with weak room-temperature conductivities (10^{-3}–10^{-4} S cm^{-1}), and their magnetic susceptibility follows a Curie–Weiss law with an effective moment of $\sim$1.5 μ_B, characteristic of one unpaired electron.

Electrodeposition at constant current from TTF and $[(C_2H_5)_4N]_3(PW_{12}O_{40})$ in acetonitrile at room temperature on a (001)-Si anode leads to a black thin film (thickness $\sim$100 μm, sample 11) [25]. Electron microscopy images shown on figure 8 evidence a thick continuous film made of stacked sheets of individual thickness ranging from 5 to 25 μm. X-ray photoelectron spectroscopic surface analysis shows two peaks at 164.2 and 248.0 eV. The first peak position is in agreement with S 2p lines of TTF derivatives and the second one has a binding energy characteristic of W $4d_{5/2}$ of W^{VI} oxides. The S/W atomic ratio of 1.92 is in agreement with a six TTF/one $PW_{12}O_{40}$ stoichiometry, as

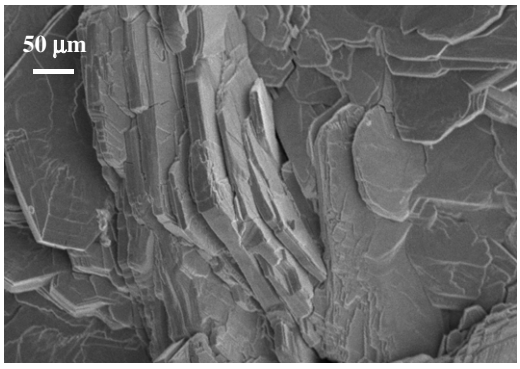

Figure 8. Scanning electron micrograph for sample 11.

previously reported for $(TTF)_6[(C_2H_5)_4N](HPW_{12}O_{40})$ single crystals grown on a Pt anode [24]. The infrared spectrum evidences ν_{CH} stretching modes in TTF (3065 cm^{-1}) and $(C_2H_5)_4N^+$ (2850–2950 cm^{-1}) moieties. Several intense features characteristic of the presence of the phosphotungstate moiety are assigned according to the literature [26]: $\nu_{as}(W–O_{term})$ = 975 cm^{-1}, $\nu_{as}(W–O–W) = 893$ cm^{-1} (bridges between corner-sharing octahedra), $\nu_{as}(W–O–W) = 803$ cm^{-1} (bridges between edge-sharing octahedra). Magnetic susceptibility measurements for the films give an effective moment of $\mu_{eff} \sim 1.5$ μ_B, a value identical to that reported for single crystals. A room-temperature conductivity of $\sim 2 \times 10^{-5}$ S cm^{-1} is obtained, to be compared to 10^{-3}–10^{-4} S cm^{-1} on single crystals. The loss of conductivity is explained by intersheet contacts which are more resistive than the material itself.

4.2. θ-$(BETS)_4[Fe(CN)_5NO]$ and $(BEDT–TTF)_4K[Fe(CN)_5NO]_2$

Crystals of θ-$(BETS)_4[Fe(CN)_5NO]$, obtained by electrocrystallization technique using standard platinum wire electrodes, appear as thick blocks and a few others as diamond and hexagonal plates. The compound behaves as a metal down to ca. 40 K with $\sigma_{RT} = 10^{-2}$ S cm^{-1}. Its crystal and electronic structures have already been reported [27]. The same cell parameters were found whatever the morphology of the crystals.

Thin films of θ-$(BETS)_4[Fe(CN)_5NO]$ are obtained by galvanostatic electrolysis on a silicon wafer in an electrochemical cell containing the BETS donor and the nitroprusside salt in a (1/10) 1,1,2-trichloroethane/ethanol solution [28]. Electron microscopy images show that the deposit uniformly covers the surface of the substrate (figure 9). It consists in a thin film made of platelets of irregular shapes but also of diamond- and hexagonal-shaped single crystals as previously evidenced. X-ray photoelectron spectroscopy analysis of the films gives atomic S/Se and Fe/N ratios of 1.09 and 0.19 respectively, in very good agreement with the theoretical values in BETS (1) and $Fe(CN)_5NO$ (0.17) moieties. The structure of the film and that of a powder obtained by electrocrystallization on a classical platinum wire electrode are analyzed by x-ray powder diffraction at room temperature. The similarity of the data (the same position for

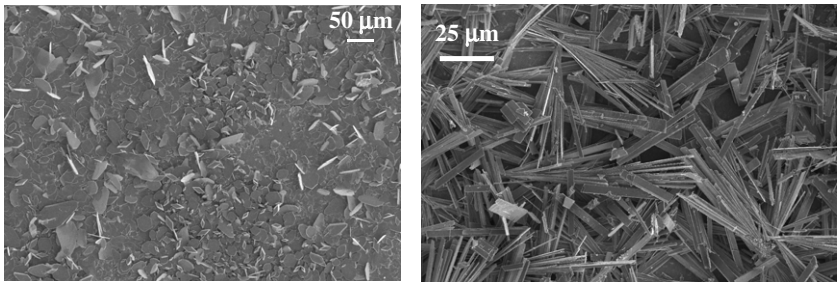

Figure 9. Scanning electron micrographs for samples 12 (left) and 13 (right).

the detected diffraction lines in film and powder) indicates that the two samples are identified with the same phase. Raman investigation confirms the presence of both the BETS and $Fe(CN)_5NO$ moieties within the deposit. The spectrum is dominated by a strong broad signal centered at 1470 cm^{-1}, which is ascribed to the stretching of the central and peripheral C=C double bonds in BETS. The conductivity, measured directly on the microcrystalline film grown on the silicon wafer, is about 1.6 S cm^{-1} at room temperature. This value is surprisingly two orders of magnitude higher than those on single crystal (10^{-2} S cm^{-1}) and compacted powder (5×10^{-2} S cm^{-1}), respectively. Despite the low conductivity of inter-fiber or inter-grain contacts within the film, this feature is attributed to the fact that the measurement on the single crystal was not performed along the most favorable conductive direction. The shape and the size ($0.4 \times 0.2 \times 0.05$ mm^3) of the crystal did not allow another orientation. In contrast, the microcrystals seem to grow on the silicon wafer in a favorable orientation versus the substrate plane. Moreover, the semiconductive thermal behavior ($E_a = 0.03$ eV) compared to the metallic one observed in the single crystal means that the overall electric behavior of the material is somewhat affected by the inter-grain contacts.

Likewise, $(BEDT\text{-}TTF)_4K[Fe(CN)_5NO]_2$ films are obtained from the oxidation of the BEDT-TTF donor in the presence of $K_2[Fe(CN)_5NO]$ in dichloromethane solution. As shown in figure 9, films consist of long needles, a morphology similar to that of single crystals previously prepared [29]. While single crystals of this phase are metallic, the film behaves as a semiconductor with a very low activation energy ($E_a = 0.006$ eV).

5. Single component conductor: $Ni(tmdt)_2$

$Ni(tmdt)_2$ is the first example of a thin film of a single component neutral molecular metal preserving its intrinsic metallic behavior [30]. $Ni(tmdt)_2$ thin films have been grown on silicon substrates from an acetonitrile solution of $[(CH_3)_4N]_2[Ni(tmdt)_2]$ by the galvanostatic technique. Due to the high air-sensitivity of $[(CH_3)_4N]_2[Ni(tmdt)_2]$, the electrodeposition has been performed in a glove box, with a current density of 2.5 $\mu A\,cm^{-2}$ at 300 K over 5 days. The polycrystalline morphology of the films is obvious on the electron microscopy image shown in figure 10. Infrared spectra and x-ray diffraction patterns confirm that the deposits

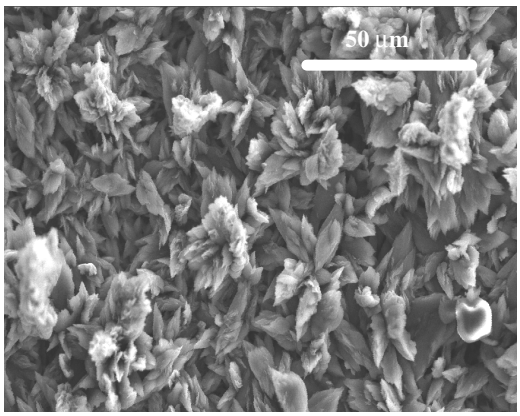

Figure 10. Scanning electron micrograph for sample 14.

are composed of $Ni(tmdt)_2$ molecules and that they crystallize in the same triclinic phase as monocrystalline $Ni(tmdt)_2$ [31]. The sample exhibits a clear metallic behavior down to 6 K with $\sigma_{RT} \sim 100$ S cm^{-1} and $\sigma_{6\,K} \sim 135$ S cm^{-1}. As expected, because of grain boundary effects, σ_{RT} is clearly lower than the conductivity values found in single crystals (400 S cm^{-1} at 300 K). The Raman spectra show the characteristic C=C $a_g\nu_3$ mode of the 'TTF moiety' at 1435 cm^{-1}, suggesting an internal charge transfer of about 0.8–0.9 in $Ni(tmdt)_2$. The experimental lineshape of high resolution x-ray photoelectron spectrum of the S 2p line can be satisfactorily decomposed in two equivalent contributions. Each contribution has two components, the more intense one corresponding to C–S–C bonding and the less intense one to C–S–Ni. These two components are shifted by 1.5 eV and each one contains two lines, $2p_{3/2}$ and $2p_{1/2}$, separated by 1.2 eV. The intensity ratio of the components, 2:1, is imposed by the chemical composition of the $Ni(tmdt)_2$ molecule. From this constraint it follows that the experimental data cannot be fitted to a single contribution. The presence of more than one contribution indicates the presence of molecules in different charge states.

6. Nanowire films

For all examples described above, thin films on silicon are made of micrometer-size crystals. Electrodeposition at constant current density from perylene (Per: $C_{20}H_{12}$) and $[(n\text{-}C_4H_9)_4N][Au(mnt)_2]$ (mnt^{2-}: maleonitriledithiolate) in

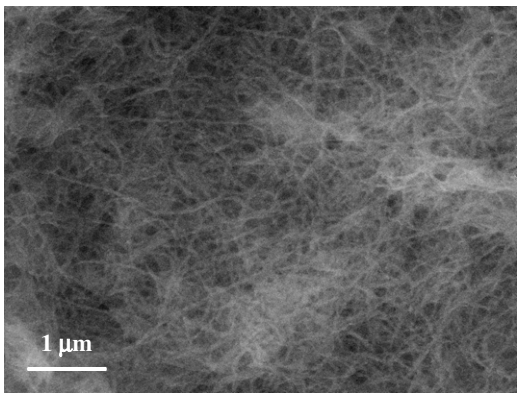

Figure 11. Scanning electron micrograph for sample 15.

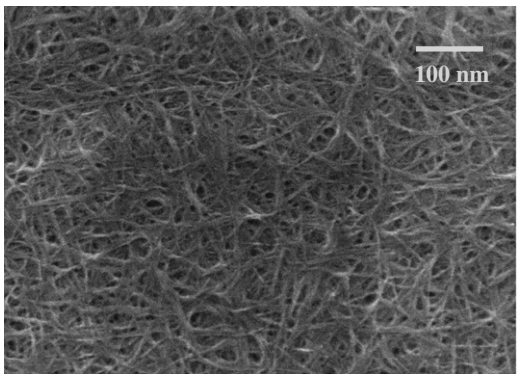

Figure 12. Scanning electron micrograph for sample 16.

dichloromethane at room temperature leads surprisingly to a film of $Per_2[Au(mnt)_2]$ made of nanowires (sample 15, figure 11) [32]. The diameter of an individual nanowire shows a low dispersity in the 35–55 nm range. Typical film thickness evaluated from the side view of the sample is about 10 μm. X-ray diffraction studies evidence that the films have either an amorphous or a nanocrystalline character, the latter being in agreement with the observation of nanowires. Elemental analysis of a sample scratched from the surface confirms a 2:1 stoichiometry. X-ray photoelectron spectroscopy confirms the presence of Au, S and N atoms within the films. The binding energy of the Au $4f_{7/2}$ peak is 86.1 eV, which can be associated with a formal Au(III) oxidation state [33]. The N 1s line is composed of a main peak located at 398.2 eV binding energy and a shoulder at ca. 401 eV. The lineshape is characteristic of the presence of the cyano group, that is composed of a main peak and a shake-up satellite. The satellite arises from the energy loss (about 3 eV) of electrons associated with the occupied–unoccupied CN-related states. The infrared spectrum evidences CH ethylenic stretching modes for perylene (3046 cm^{-1}) and CN stretching modes for the nitrile groups of mnt^{2-} ligands (2208 and 2220 cm^{-1}). The electrical conductivity of $Per_2[Au(mnt)_2]$ nanowire films is about 0.02 S cm^{-1} at room temperature and follows a thermally activated behavior ($E_a = 88$ meV). This unexpected preparation of $Per_2[Au(mnt)_2]$ nanowires encouraged us to develop selective processing of nanowire films. Recently, nanowire arrays of $[(CH_3)_4N][Ni(dmit)_2]_2$ have been fabricated by galvanostatic electrochemical deposition using anodic aluminum oxide as the template [34]. These nanowire arrays actually consist of nanopearl chains and are highly textured as determined by x-ray diffraction studies. However, the preparation of the porous alumina is not straightforward. The prepared template has to be metallated to be used as a working electrode. We have preferred to use another type of template, i.e. a Si-supported multilamellar membrane, prepared following a procedure described by Li *et al* [35]. These well ordered multilamellar templates are easily produced by spreading small drops of a lipidic solution on Si surfaces and letting the solvent evaporate slowly. The phospholipid used ($DC_{8,9}PC$) contains a zwitterion type headgroup and two long alkyl chains [35, 36]. Each alkyl chain has two conjugated carbon–carbon triple bonds which can polymerize by irradiating with a UV light. This template, used as a working electrode, preserves its lamellar structure in the electrolyte solution. It was advantageously used for growing nanowires of $(EDT\text{-}TTFVO)_4(FeCl_4)_2$ (EDT-TTFVO: ethylenedithiotetrathiafulvalenoquinone-1,3-dithiolemethide). This fractional oxidation state conductor is obtained as large single crystals on a silicon electrode [32]. Using a Si-supported multilamellar membrane as electrode, growth as nanowires is conceivable as follows: EDT-TTFVO molecules migrate from the solution/membrane interface to the substrate surface via the channels delimited by the long alkyl chains. They are oxidized and produce the conducting salt by combination with $FeCl_4^-$ ions, largely present in the vicinity of the hydrophilic silicon surface. As the growing salt is in contact with $FeCl_4^-$ ions located in inter-headgroup areas, the growth can continue but should adapt to nanometric size of the channels. Even when the growing salt reaches the membrane surface, the growth still continues towards the formation of long nanowires lying parallel to the membrane surface, as evidenced by scanning electron microscopy (figure 12). We currently study the I–V curves of individual nanowires after extracting them from the surface, as previously reported for other conducting nano-objects [37].

7. Growth mechanism approach

Various factors influence the structurization of the film on the substrate surface. First of all, the surface morphology of the substrate is of great importance as it governs the nucleation mechanism. During electrodeposition, the potential applied to an ideally flat electrode is equally distributed over the surface. Only corners and edges may support higher potentials and crystal growth often occurs at these substrate locations. Any imperfection of the substrate surface also favors localized crystal growth. It is possible to avoid localized nucleation by equalizing the charge distribution on the substrate surface. This can be done by applying chemical etching treatments to the substrate before its use [38]. Depending on the treatment, the structuration produces cavities of various sizes and shapes. The nucleation equally takes place within these cavities, which act as micro- or nanoflasks. We have observed a direct relationship between the size of the cavities and that of the nucleates: microsize cavities lead to micrograins or microfibers, and nanocavities favor the growth of nanocrystallites. This

indicates that the surface morphology has a templating effect on the morphology of the deposit. This effect can be compared to the epitaxial influence of the substrate on the structure of chemically vapor deposited films. The templating effect of the substrate can be enhanced by using organized layers as reported in the previous section. Another important parameter to be controlled in electrodeposition is the current density. For a given structured surface, low current densities favor the growth of few nucleates which further develop, whereas higher current densities favor a larger number of nucleates of smaller size. In general, one-dimensional molecular conductors grow as needles along the highest conductive pathway of their structural organization. Therefore, micro- or nanofibers develop from nucleates of similar size because, as soon as they fill all micro- or nanoflasks, these nucleates are more conductive than the substrate and act as micro- or nanoelectrodes.

8. Conclusion

We have reviewed examples of the feasibility of producing thin films of molecule-based conductors by electrodeposition. We have explored the use of silicon substrates, whose importance in the electronic domain is obvious. Within the dithiolato-bearing complexes, we have seen that, although films of TTF[Ni(dmit)$_2$]$_2$ and Ni(tmdt)$_2$ exhibit a polycrystalline morphology, they show metal-like behavior down to low temperatures. In the first compound, the superconducting transition has been evidenced on the film. This is the second example after that reported by Laukhina *et al* on vapor-grown β-(BEDT-TTF)$_2$I$_3$ films [39], and the first including a transition metal complex. For M(dcbdt)$_2$ complexes, the electrodeposition method allowed isolation of (TMTSF)$_x$[M(dcbdt)$_2$]$_y$ derivatives, whereas standard electrocrystallization was not successful. In the case of the θ-(BETS)$_4$[Fe(CN)$_5$NO] compound, the orientation and the two-dimensional growth of the film on the silicon surface acted in favor of better conductive properties by comparison with single crystals. The silicon electrode could occasionally lead to nanowire-containing films, as seen for Per$_2$[Au(mnt)$_2$]. However, the use of Si-supported multilamellar templates to prepare films of (EDT-TTFVO)$_4$(FeCl$_4$)$_2$ favored the selective growth of nanowires. This technique appears to be the most suitable for preparing a large variety of molecule-based conductors exhibiting a nanowire-like morphology. Nanometric-structured molecule-based conductors could be indeed found at the forefront of the scene because of their novel properties and potential applications.

Acknowledgments

The work reviewed here issues from the 'Molecules and materials' group and benefits from collaborations with the below cited groups. It has been carried out with financial support of various institutions and programs: CNRS exchange programs (CNRS-RAS, CNRS-AIST), COST D14, and ATUPS fellowships from Université Paul Sabatier in Toulouse. J-P Savy thanks the Fond Social Européen (FSE) for a PhD grant. The authors appreciate the contribution and collaboration of the following persons: C Routaboul (Raman), V Collière (electron microscopy), F Senocq (powder x-ray diffraction), J Fraxedas (x-ray photoelectron spectroscopy), C Faulmann (resistivity measurements), P Auban-Senzier and C Pasquier (resistivity measurements in the superconducting domain), J-C Coiffic, E S Choi and J S Brooks (resistivity measurement on (TMTSF)$_2$ClO$_4$), M Almeida (dcbdt^{2-} and mnt^{2-} complexes), L Ouahab (polyoxometalates), A Mari and J-F Meunier (magnetic susceptibility measurements), L Pilia, L A Kushch and E B Yagubskii (donor/photochromic ions), J-M Fabre (tmdt^{2-} ligand) amd T Sugimoto (EDT-TTFVO precursor).

References

[1] Cassoux P, Valade L and Fabre P-L 2003 *Comprehensive Coordination Chemistry II: From Biology to Nanotechnology* vol 1, ed J A McCleverty and T J Meyer (Amsterdam: Elsevier) p 761
[2] Batail P, Boubekeur K, Fourmigué M and Gabriel J-C P 1998 *Chem. Mater.* **10** 3005
[3] Hillier A C, Maxson J B and Ward M D 1994 *Chem. Mater.* **6** 2222
[4] Liu S G, Wu P J, Liu Y Q and Zhu D B 1996 *Mol. Cryst. Liq. Cryst.* **275** 211
[5] Miura Y F, Tovar G E M, Ohnishi S, Hara M, Sasabe H and Knoll W 2001 *Thin Solid Films* **393** 225
[6] Wang H H, Stamm K L, Parakka J P and Han C Y 2002 *Adv. Mater.* **14** 1193
[7] Wang H H, Han C Y, Noh D-Y, Shin K-S, Willing G A and Geiser U 2003 *Synth. Met.* **137** 1201
[8] Cassoux P and Valade L 1996 *Inorganic Materials* ed D W Bruce and D O'Hare (New York: Wiley) p 1
[9] Brossard L, Ribault M, Valade L and Cassoux P 1986 *Physica* B **143** 378
[10] de Caro D, Fraxedas J, Faulmann C, Malfant I, Milon J, Lamère J-F, Collière V and Valade L 2004 *Adv. Mater.* **16** 835
[11] Savy J-P, de Caro D, Valade L, Legros J-P, Auban-Senzier P, Pasquier C R, Fraxedas J and Senocq F 2007 *Europhys. Lett.* **78** 37005
[12] Siedle A R 1982 *Extended Linear Chain Compounds* vol 2, ed J S Miller (New York: Plenum) p 469
[13] Brossard L, Ribault M, Valade L and Cassoux P 1990 *Phys. Rev.* B **42** 3935
[14] Bechgaard K, Carneiro K, Olsen M, Rasmussen F B and Jacobsen C S 1981 *Phys. Rev. Lett.* **46** 852
[15] Ribault M and Moradpour A 1998 *J. Am. Chem. Soc.* **120** 7993
[16] Angelova A, Moradpour A, Auban-Senzier P, Akaaboune N and Pasquier C 2000 *Chem. Mater.* **12** 2306
[17] Valade L, de Caro D, Savy J-P, Malfant I, Faulmann C, Almeida M, Fraxedas J and Brooks J S 2006 *J. Low Temp. Phys.* **142** 393
[18] Deluzet A, Perruchas S, Bengel H, Boubekeur K, Batail P, Molas S and Fraxedas J 2002 *Adv. Funct. Mater.* **23** 123
[19] Fraxedas J 2006 *Molecular Organic Materials: From Molecules to Crystalline Solids* (Cambridge: Cambridge University Press)
[20] Alves H, Simão D, Lopes E B, Belo D, Gama V, Duarte M T, Novais H, Henriques R T and Almeida M 2001 *Synth. Met.* **120** 1011
[21] Alves H, Santos I C, Lopes E B, Belo D, Gama V, Simão D, Novais H, Duarte M T, Henriques R T and Almeida M 2003 *Synth. Met.* **133** 397

[22] de Caro D, Alves H, Almeida M, Cailleux S, Elgaddari M, Faulmann C, Malfant I, Senocq F, Fraxedas J, Zwick A and Valade L 2004 *J. Mater. Chem.* **14** 2801
[23] Ouahab L 1998 *C. R. Acad. Sci. Paris* IIc **1** 369
[24] Ouahab L, Bencharif M, Mhanni A, Pelloquin D, Halet J-F, Peña O, Padiou J, Grandjean D, Garrigou-Lagrange C, Amiell J and Delhaes P 1992 *Chem. Mater.* **4** 666
[25] Caillieux S, de Caro D, Valade L, Basso-Bert M, Faulmann C, Malfant I, Casellas H, Ouahab L, Fraxedas J and Zwick A 2003 *J. Mater. Chem.* **13** 2931
[26] Rocchiccioli-Deltcheff C, Fournier M, Franck R and Thouvenot R 1983 *Inorg. Chem.* **22** 207
[27] Sanchez M E, Doublet M-L, Faulmann C, Malfant I, Cassoux P, Kushch L A and Yagubskii E B 2001 *Eur. J. Inorg. Chem.* **11** 2797
[28] Pilia L, Malfant I, de Caro D, Senocq F, Zwick A and Valade L 2004 *New J. Chem.* **28** 52
[29] Kushch L A, Buravov L, Tkacheva V, Yagubskii E B, Zorina L V, Khasanov S S and Shibaeva R P 1999 *Synth. Met.* **102** 1646
[30] Malfant I, Rivasseau K, Fraxedas J, Faulmann C, de Caro D, Valade L, Kaboub L, Fabre J-M and Senocq F 2006 *J. Am. Chem. Soc.* **128** 5612
[31] Tanaka H, Okano Y, Kobayashi H, Suzuki W and Kobayashi A 2001 *Science* **291** 285
[32] Savy J-P, de Caro D, Faulmann C, Valade L, Almeida M, Koike T, Fujiwara H, Sugimoto T, Fraxedas J, Ondarçuhu T and Pasquier C 2007 *New J. Chem.* **31** 519
[33] Pireaux J-J, Liehr M, Thiry P A, Delrue J-P and Caudano R 1984 *Surf. Sci.* **141** 221
[34] Cui G, Xu W, Guo C, Xiao X, Xu H, Zhang D, Jiang L and Zhu D 2004 *J. Phys. Chem.* B **108** 13638
[35] Xing L L, Li D P, Hu S X, Jing H Y, Fu H, Mai Z H and Li M 2006 *J. Am. Chem. Soc.* **128** 1749
[36] Seul M and Sammon M J 1990 *Thin Solid Films* **185** 287
[37] de Caro D, Sakah J, Basso-Bert M, Faulmann C, Legros J-P, Ondarçuhu T, Joachim C, Ariès L, Valade L and Cassoux P 2000 *C. R. Acad. Sci. Paris.* IIc **3** 675
[38] Kelly J J and Vanmaekelbergh D 2002 *Electrochemistry of Nanomaterials* ed G Hodes (Weinheim: Wiley–VCH) p 103
[39] Laukhina E E, Merzhanov V A, Pesotskii S I, Khomenko A G, Yagubskii E B, Ulanski J, Kryszewski M and Jeszka J K 1995 *Synth. Met.* **70** 797